Supporting Info for

Wintertime lake drainage cascade triggers large-scale ice flow response in Greenland

Authors:

Nathan Maier[1,2*], Jonas Kvist Andersen[3], Jeremie Mouginot[1,4], Florent Gimbert[1] and Olivier Gagliardini[1]

Affiliations:

[1]Univ. Grenoble Alpes, CNRS, IRD, Grenoble INP, IGE, 38000 Grenoble, France

[2]Los Alamos National Lab, Los Alamos, NM 87544,USA

[3]DTU Space, Tech. Univ. of Denmark, 2800 Kgs. Lyngby, Denmark

[4]Depart. of Earth System Science, Univ. of California- Irvine, Irvine CA 92697, USA

[*]Corresponding Author Email: ntmaier@gmail.com

Supporting Information

1 Supporting Methods

1.1 DInSAR Velocities and Annual Impact

To process the interferograms, the 2016-2019 multi-year average velocity map was generated through PROMICE (Solgaard et al., 2021) and the TanDEM-X Digital Elevation Model were used for image coregistration and phase flattening respectively. Interferograms are multi-looked with a factor of 15 x 3 in range/azimuth and unwrapped using a Minimum Cost Flow algorithm. The resulting 6-day LoS velocity maps have a pixel spacing of 50 m x 50 m and measurements from all tracks are resampled to the same (50 m x 50 m) grid. The DTU IPP software (Kusk et al., 2018) is used for all interferometric processing steps.

In some cases, we use flow-projected velocities where LoS measurements are projected onto the flow direction obtained by the 2016-2019 multi-year average velocity map (Solgaard et al., 2021), assuming that all motion is horizontally derived. This is used to compare the increased displacement resulting from the winter drainage to the multi-year average velocity (*Fig. S9*) to estimate the effect the event had on annual dynamics. We note we use the multiyear velocity average instead of using the full 2018 annual velocity series because the later cannot be resolved using DInSAR due to decorrelation during summer. Thus, this reflects increased displacement of the drainage event compared to a "typical year" average velocity. Because the flood wave causes uplift and downlift as it moves into a region and then passes, the integrated displacement of the flow projected velocities will mostly reflect horizontal motion.

1.2 Estimating Approximate SGL Volumes

Depth retrieval based on empirical (Legleiter et al., 2014) or physical (Pope et al., 2016) multi-spectral methods cannot be applied to estimate SGL volumes due to the presence of an ice lid during winter. Examining the near 50-year time series (described below) also shows that many of the high elevation lakes never become ice-free even during summer. To circumvent these limitations and roughly estimate total SGL volume prior to drainage we interpolate the sub-lake bathymetry from 2 m resolution ArcticDEMs (Morin et al., 2016). We start by manually digitizing each lake-outline along the visible edge of the ice lid and remove this area from a corresponding ArcticDEM strip collected between 2013 and 2017 during times where the lake volume is inferred to be lower or similar to that during the 2018 winter. We then interpolate a lake bathymetry using a spline (MATLAB curve fitting toolbox, smoothing parameter 0.9) over seven SGL cross sections (*Fig. S12*). The fit relies on the local slope adjacent to the ice basin to estimate the lake depth (*Fig. S13*). The maximum lake depths agree well with those found by other methods (~4-10 m) (Legleiter et al., 2014; Pope et al., 2016). The ice lid elevation is estimated using the median of the intersecting points between the lake outline and the DEM. We can then estimate the lake volume by assuming a lid thickness of ~2 m which has been observed (Lampkin et al., 2020) and modeled (Law et al., 2020) at the end of winter and then integrate the volume at each DEM grid cell. We note that even though the method has high uncertainty, it overcomes the limitations of winter imagery while still being empirically based. We test the sensitivity of the volume estimates by repeating the procedure using 8 different DEMs for Lake 2 and show a consistency of +/- 11%. We note most of the lakes are identified with collapsed ice lids, such that actual volume of water that makes it to the bed cannot be confidently estimated, as some of the lakes may have only partially drained. Thus, we interpret these estimates as rough volume maximums which could have drained to the bed.

1.3 Interpreted Drainage Pathways

The decomposed velocity components demonstrate that the complex structure is a result of vertical uplift (*Fig. 2*) which were interpreted to represent primary drainage pathways. Using this interpretation, we manually delineate the major flow pathways using a map of the maximum LoS velocities recorded during the event, which retains the complex structure from the drainage site to the margin (*Fig. S4*). Two major westward pathways, one major northward drainage pathway, a secondary drainage pathway from the lake drainages that occur just upgradient of the Nordenskiöld trough, and a connector between the secondary and primary westward drainage pathways are identified.

1.4 Drainage Velocities

We track the wave front and peaks for consecutive DInSAR velocity maps (using track T90) to determine the position of the velocity wave through time along inferred drainage pathways. The wave front is defined as the first location on the ascending limb of the wave where LoS velocities are 10% higher than pre-drainage velocities. The wave peak is taken as the flowline maximum. We then differentiate the wave fronts or peaks between two consecutive flowline velocity profiles to get the distance traveled which is converted to velocity using the 6-day repeat period (*Fig. 3*).

1.5 Long-term SGL Evolution

We document the evolution of the surface area for the 15 supraglacial lakes identified to drain during the event over the last 50 years. We downloaded 1275 optical images from the Landsat satellite record that began in 1972 (only 1983 onward is shown in *Fig. 4*), built a stack of sub-images for each lake and manually digitized their outline twice a year when possible, before May/June when the melt season begins and a second time between August and November at the end of the melt season. We then calculated the evolution of the area of the lakes (*Fig. 4*) through time to establish the historical context of the SGL evolution preceding the winter drainage event.

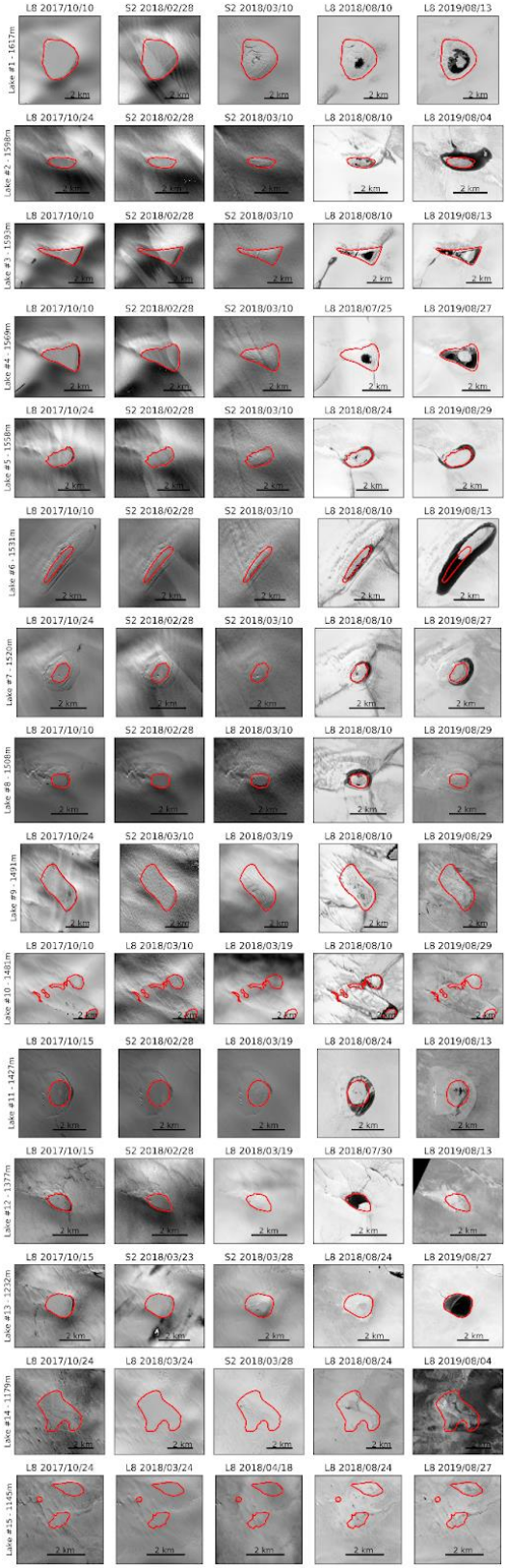

Figure S1 - Lake evolution before and after the drainage from Landsat (L8) and Sentinel-2 (S2) optical images. The red outlines indicate the lake perimeters in fall 2017 prior to the event.

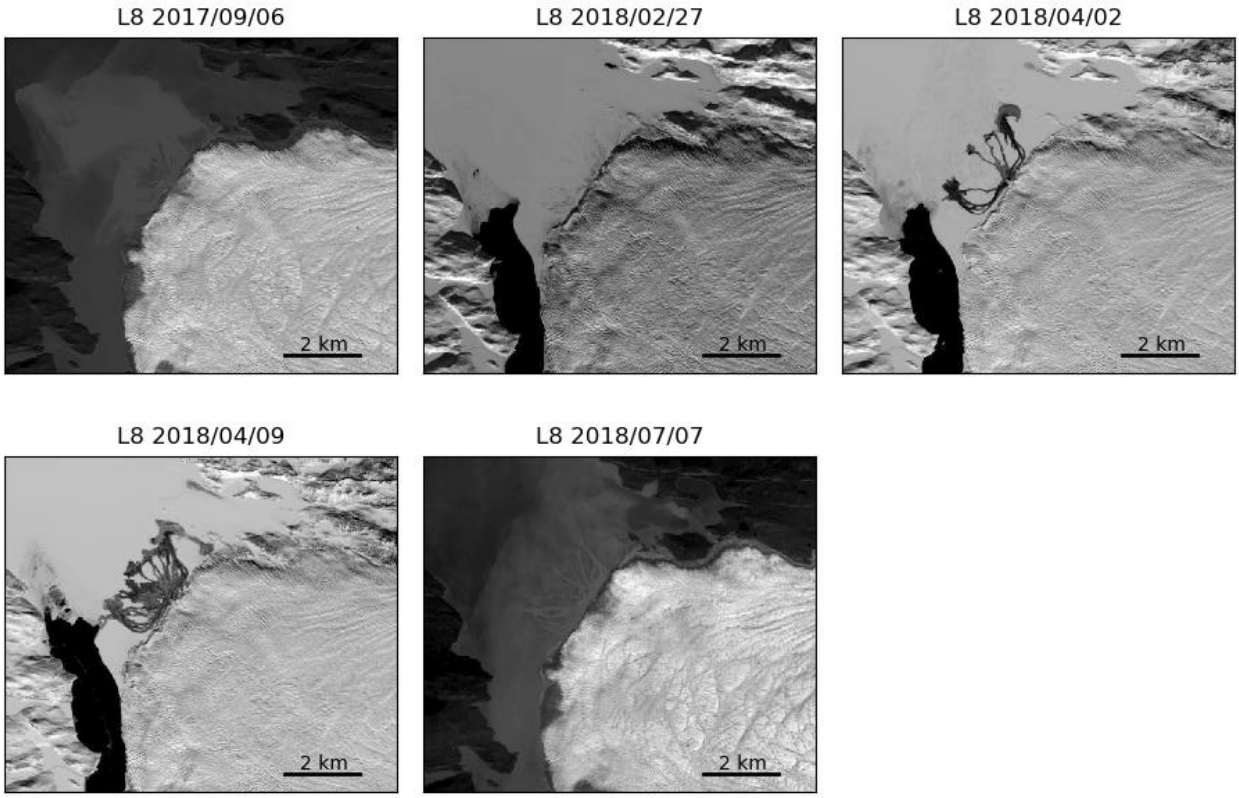

Figure S2 – Landsat images of the Nordenskiöld ice tongue showing the outwash in early April 2018 following supraglacial lake drainages. At this time of the year the surface of the sedimentary delta in front of Nordenskiöld is covered with snow, making it possible to clearly identify the areas swept by the flow.

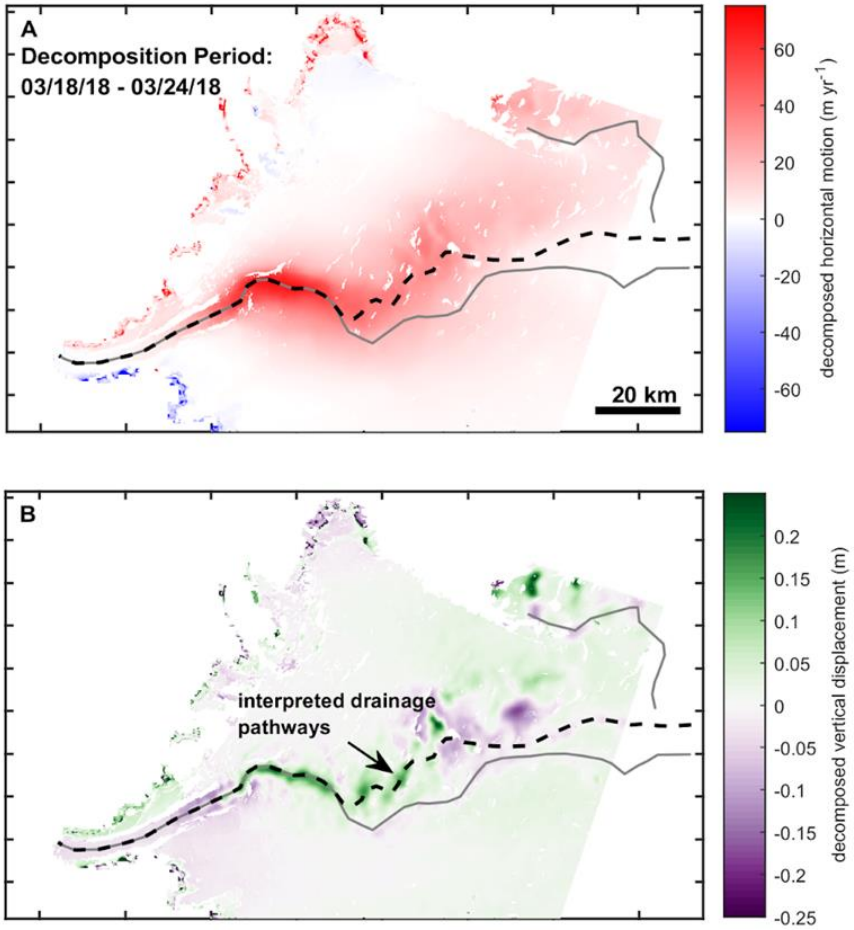

Figure S3 – Decomposed motion – Snapshot (03/18/18 - 3/24/18) of decomposed horizontal motion (relative to pre-drainage velocities) (**A**) and vertical surface displacement (**B**) during drainage event. This snapshot follows that presented in Figure 2.

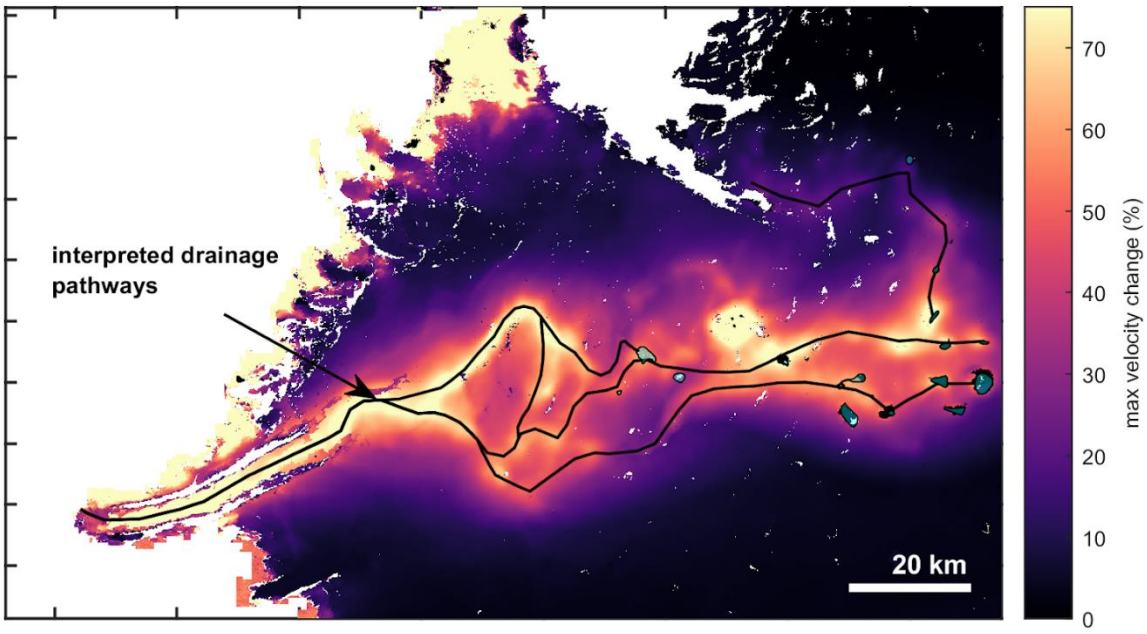

Figure S4 – Interpreted Drainage Pathways – Complex structure from max flow projected velocities during drainage event (Track 90) were used to visually interpret inferred drainage pathways (black lines). Cyan fill shows drained lake locations.

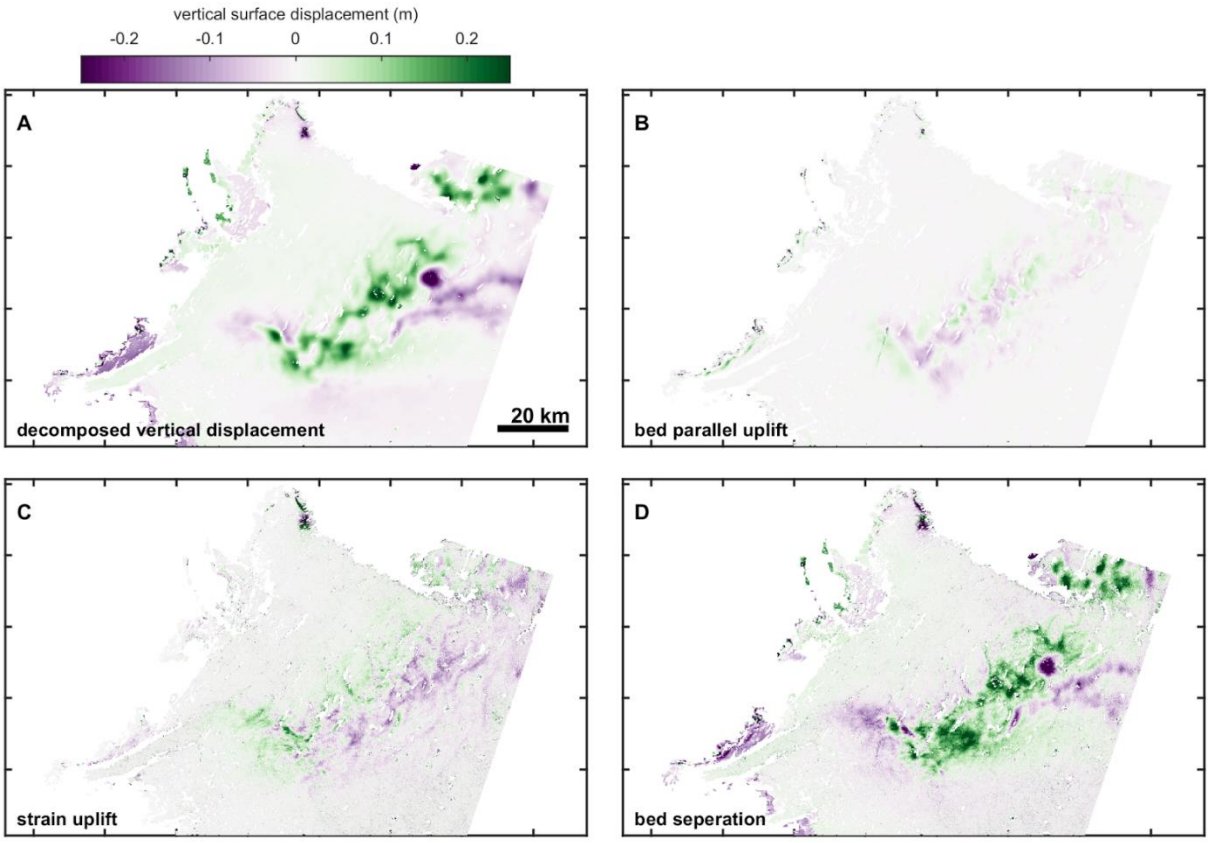

Figure S5 – Vertical surface displacement components – Decomposed vertical motion during drainage event (centered around 10.6 days after initial drainage using Track 90 and 25 velocities spanning from March, same as Fig. 2 in the main text) (**A**), bed parallel uplift (**B**), vertical displacement due to vertical strain (**C**), and bed separation (**D**). Vertical strain and bed parallel uplift were estimated with the decomposed horizontal velocity assuming changes in motion are derived from sliding. Bed separation is taken as the residual between the decomposed vertical motion and the bed parallel and vertical strain uplift.

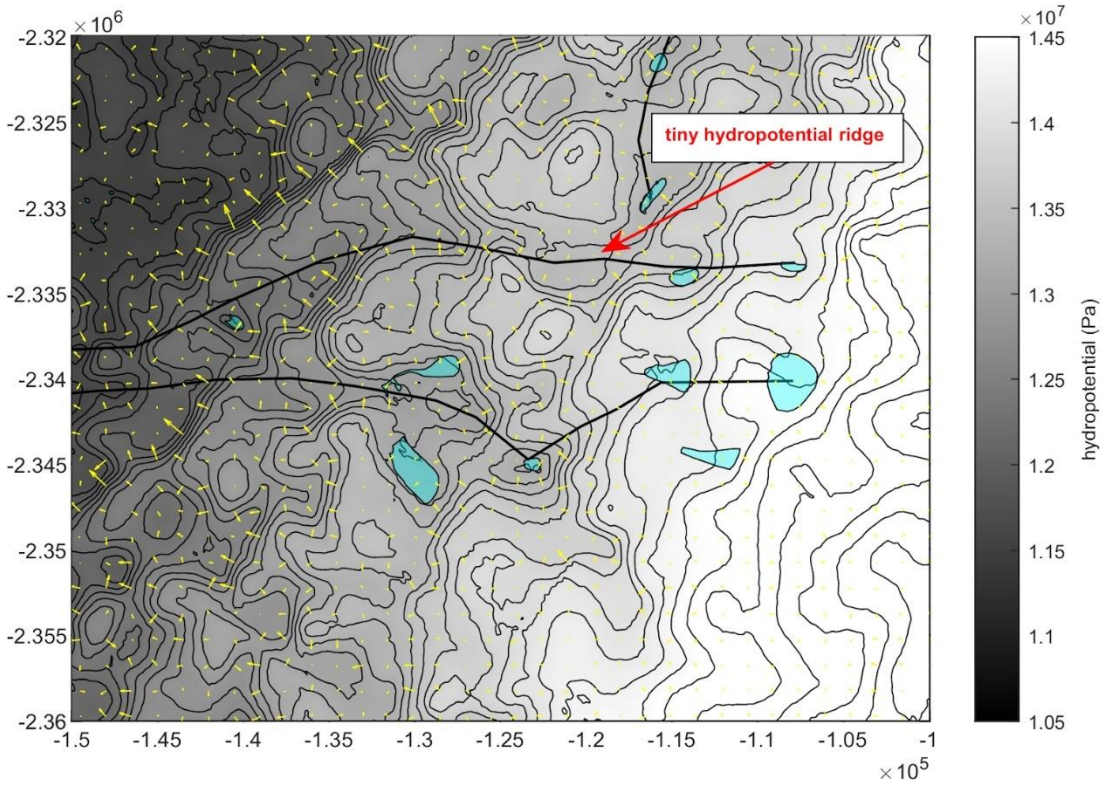

Figure S6 – Zoom of hydropotential for a region that incorporates the start of three major inferred drainage pathways. The two westward propagating drainage pathways are separated from the northernmost hydropotential pathway by a small ridge of high pressure (arrow). Hydropotential gradients were calculated assuming ice overburden pressure and hydropotential gradients (yellow vectors). Cyan regions show locations of supraglacial lakes that drained during the event. Contours of hydropotential (black lines) spaced 150 kPA apart are presented to better show troughs and ridges in the hydropotential field.

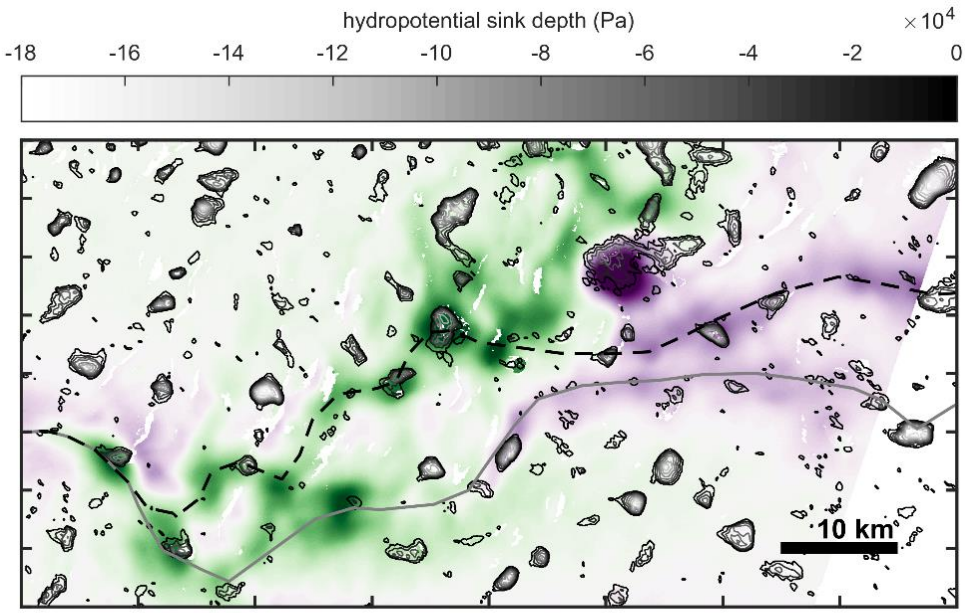

Figure S7 – Bead and thread uplift structure in relation to subglacial sinks and interpreted flowlines (same as shown on Fig. 2). Subglacial sinks are delineated with hydropotential contours calculated assuming ice overburden pressure.

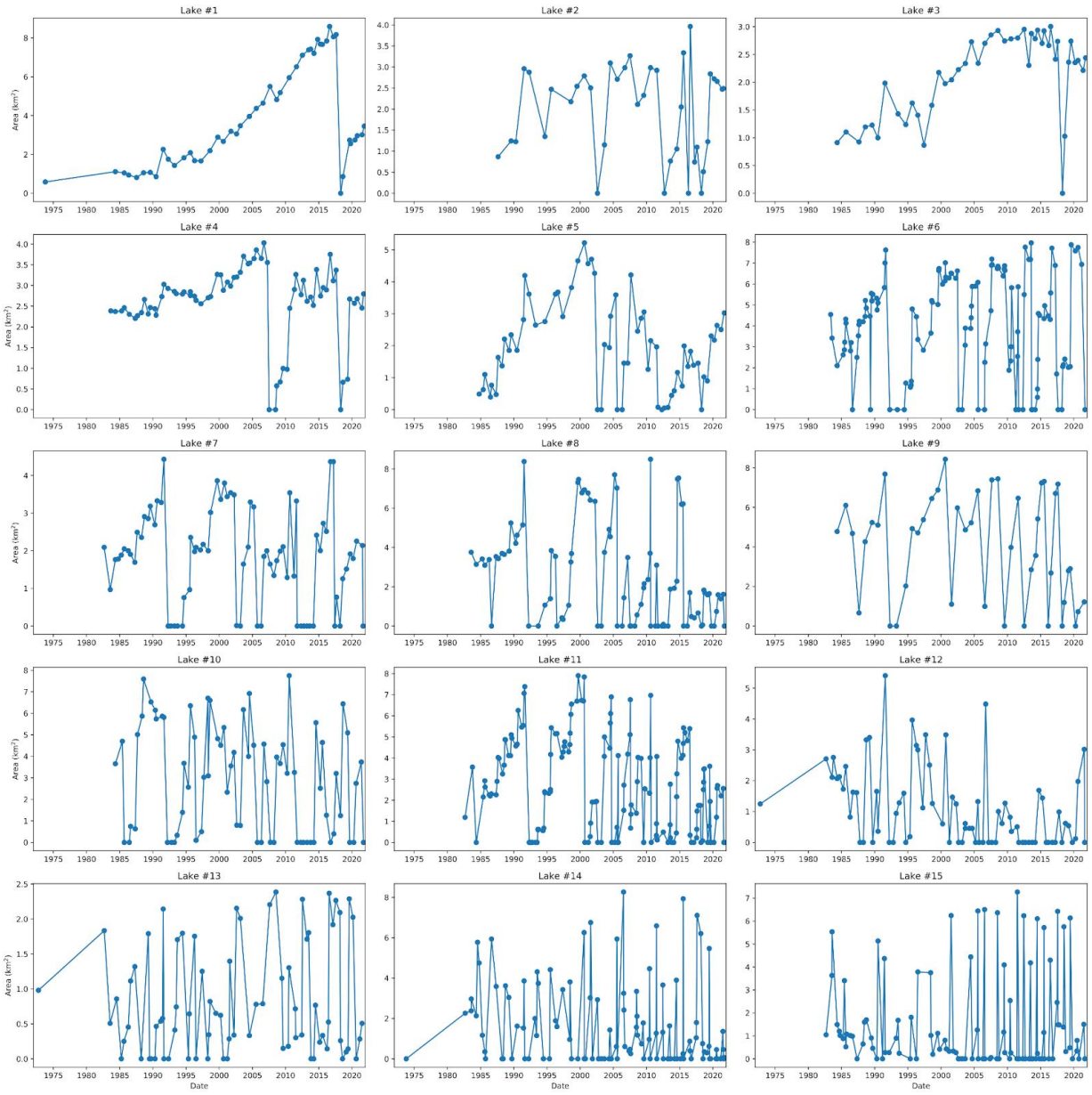

Figure S8 – The area of lakes that drained during the event is plotted as a function of time.

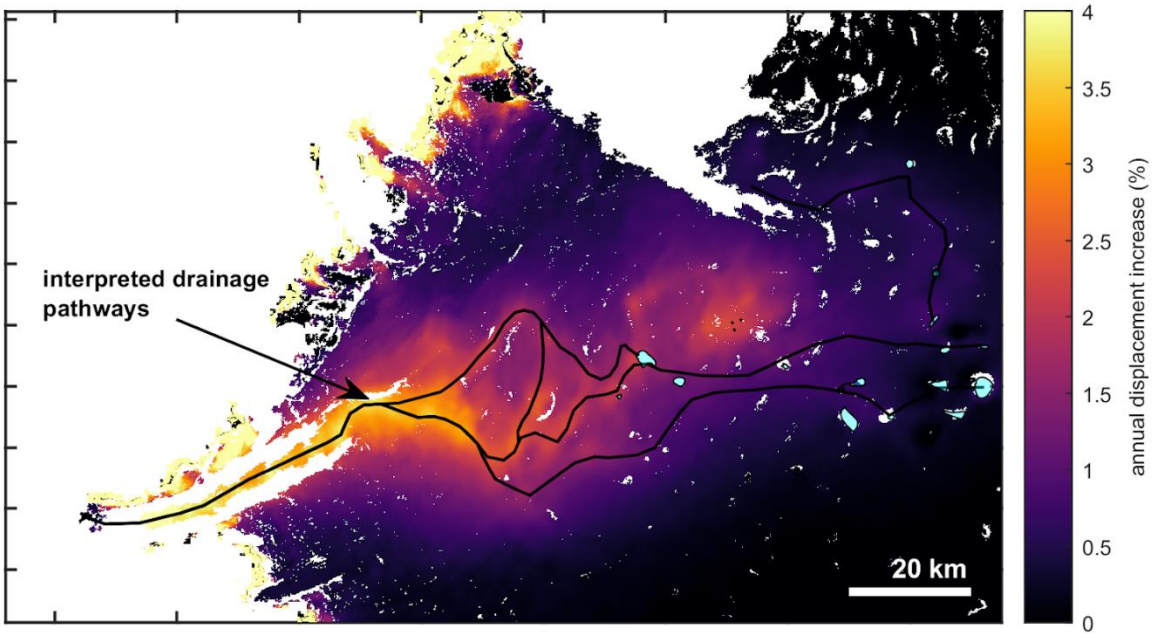

Figure S9 – Percent increase in annual velocity due to elevated velocities during the event. Black lines show inferred flow pathways. Increase was calculated using multi-year average annual displacement from 2016-2019 (Solgaard et al., 2021) and comparing it to increased displacement during the drainage event (*SI*).

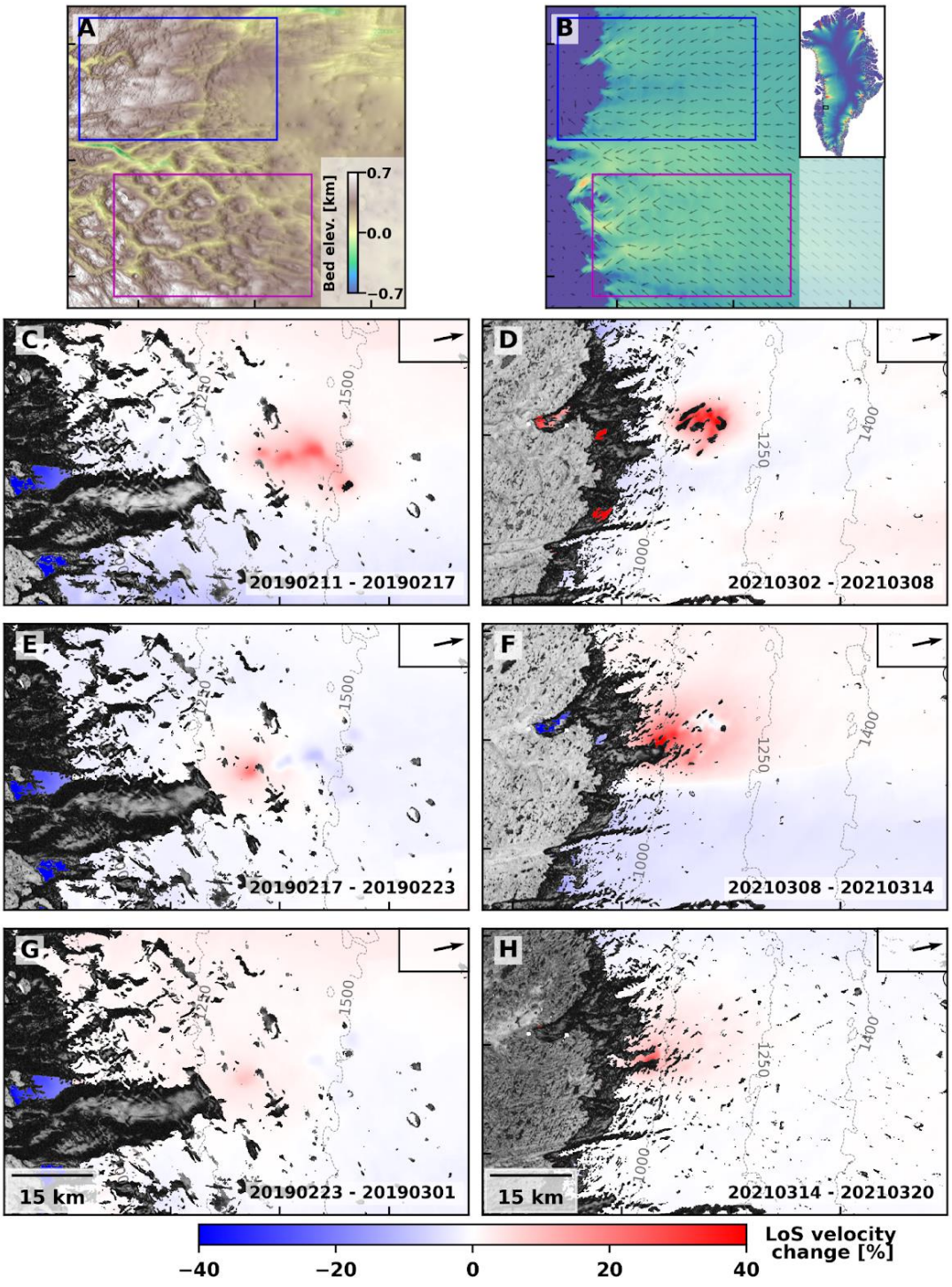

Figure S10 – Dynamic response to lake drainages identified during February 2019 40 km south of Russell Glacier (**C**,**E**,**G**) and March 2021 50 km north of Russell Glacier (**D**,**F**,**H**) measured with Sentinel-1 DInSAR (track 90) consecutive 6-day pairs. Panels (**C**)-(**H**) show the relative change in line-of-sight velocity (in percent) with respect to a pre-event acquisition overlayed on the coherence for the respective image pair. Panels (**A**) and (**B**) show bed elevation and 1995-2016 average velocity in the region of the 2019 event (magenta rectangle) and the 2021 event (blue rectangle).

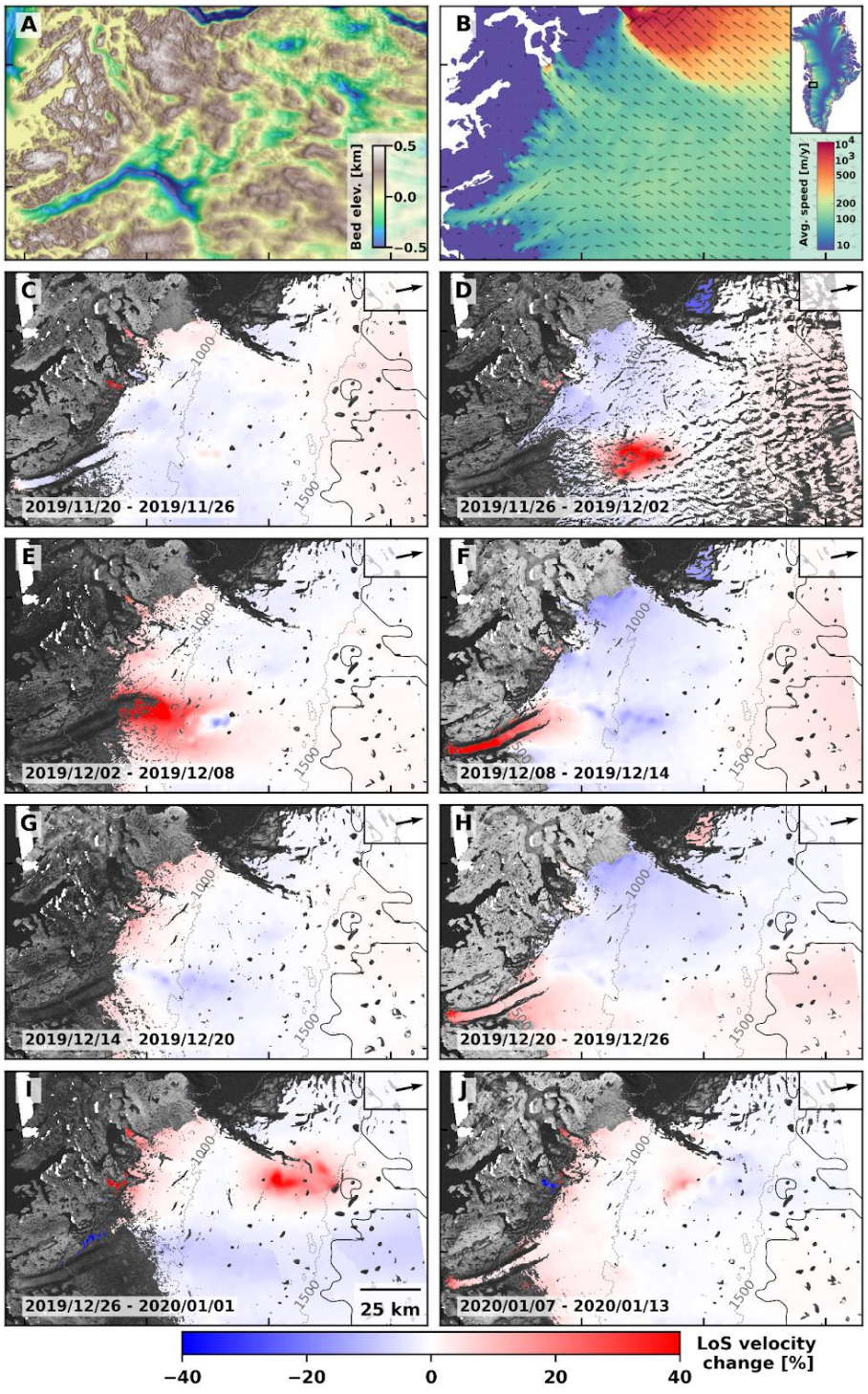

Figure S11 – Dynamic response to two additional lake drainages identified during early December 2019 (**C**,**E**,**F**) and late December 2019 (**H, I, J**) measured with Sentinel-1 DInSAR (track 90) consecutive 6-day pairs. Panels (**C**)-(**H**) show the relative change in line-of-sight velocity (in percent) with respect to a pre-event acquisition overlayed on the coherence for the respective image pair. Panels (**A**) and (**B**) show bed elevation and 1995-2016 average velocity in the region of the 2019 event.

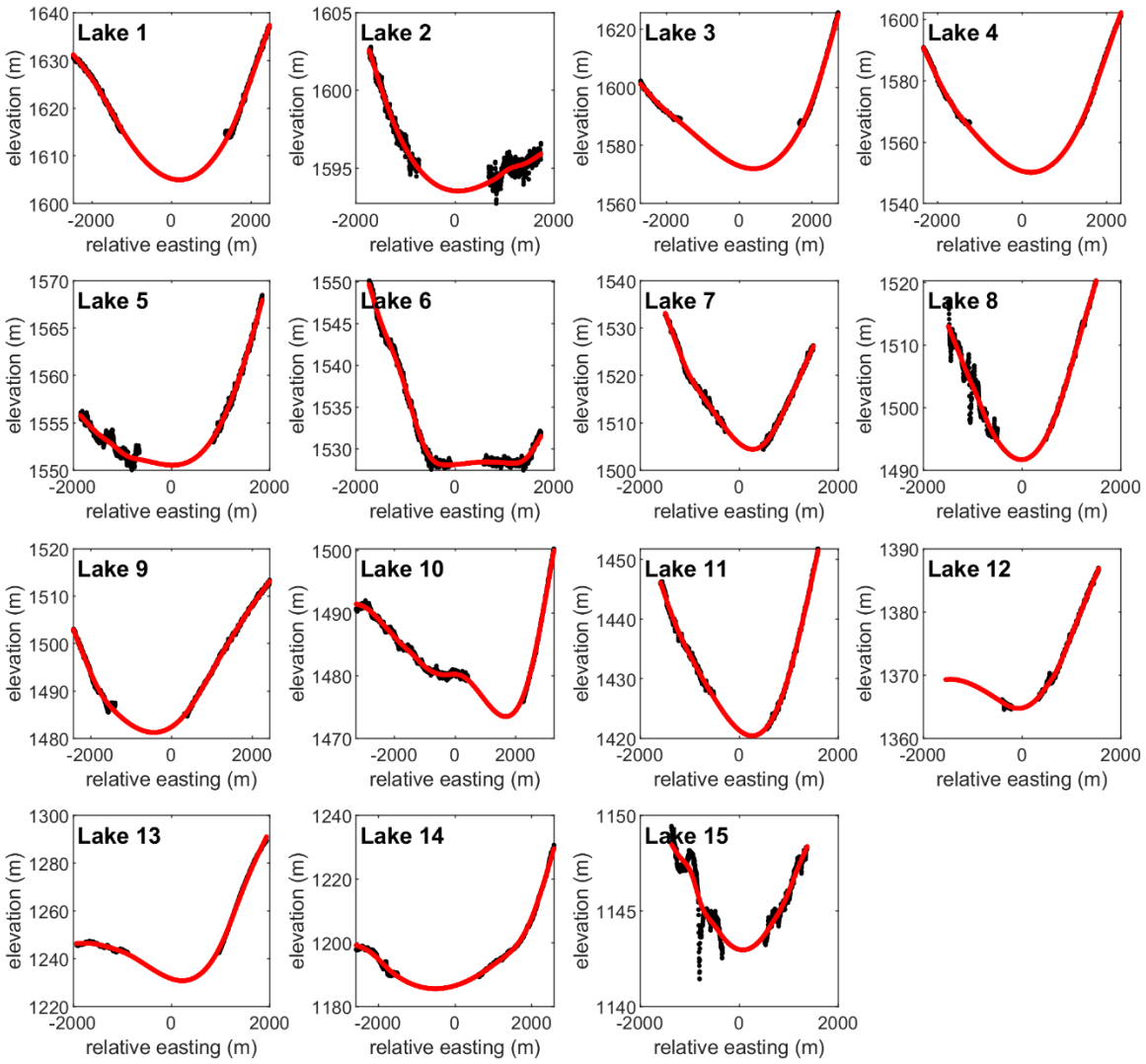

Figure S12 – Spline lake-bottom interpolation. Two-dimensional cross section of smoothing spline (red line, smoothing parameter = 0.9) fit through ArcticDEM (Morin et al., 2016) elevation data (black line) for all 15 lakes.

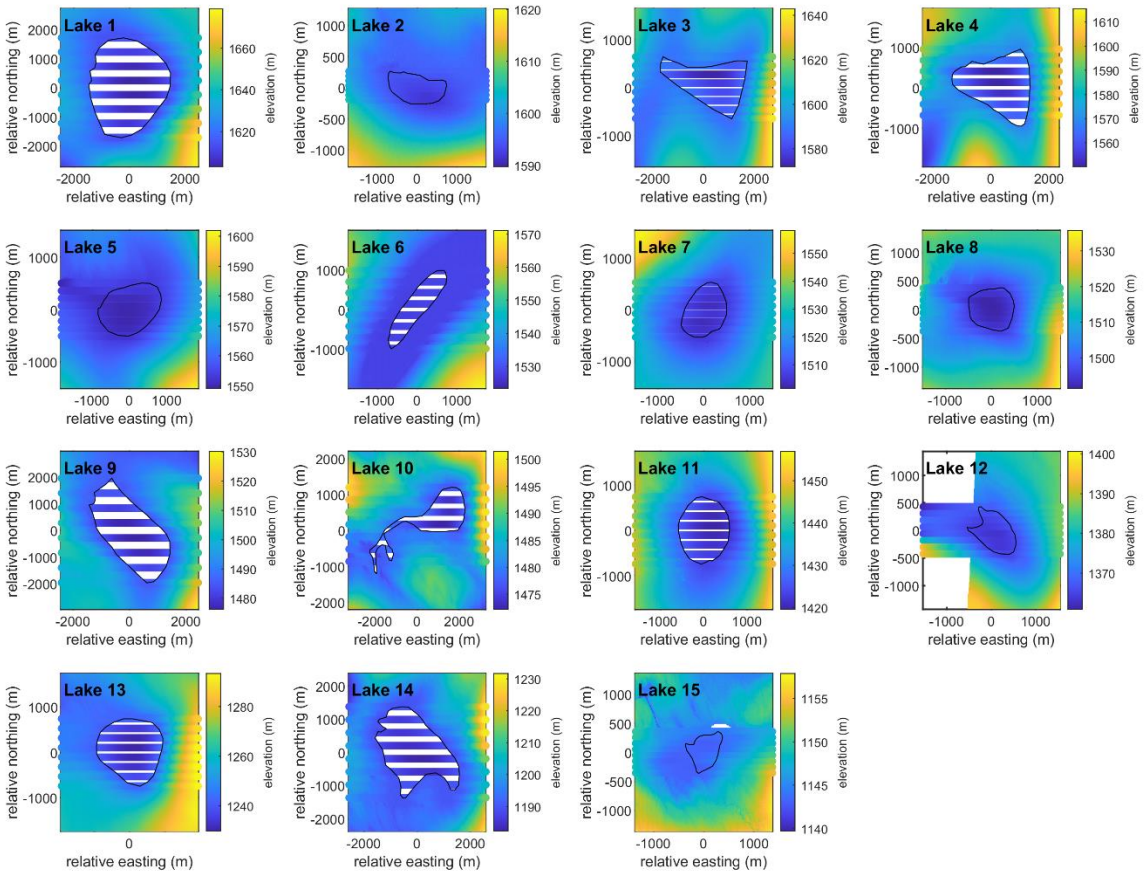

Figure S13 – Map view of spline lake-bottom interpolation. Map view of smoothing splines (horizontal lines, smoothing parameter = 0.9) fit through ArcticDEM (Morin et al., 2016) elevation data (background data) for all 15 lakes.